2011

Radar characteristics of continental, coastal, andmaritime convection observed during AMMA/NAMMA

Nick Guy
Colorado State University - Fort Collins, guy@atmos.colostate.edu

Steven A. Rutledge
Colorado State University - Fort Collins

Robert Cifelli
NOAA/Earth System Research Laboratory

RMetS
Royal Meteorological Society

Radar characteristics of continental, coastal, and maritime convection observed during AMMA/NAMMA

Nick Guy,[a]* Steven A. Rutledge[a] and Robert Cifelli[b]
[a]*Department of Atmospheric Science, Colorado State University, Fort Collins, Colorado, USA*
[b]*Cooperative Institute for Research in the Atmosphere, Colorado State University, and NOAA/Earth System Research Laboratory, Boulder, Colorado, USA*
*Correspondence to: N. Guy, Colorado State University, Department of Atmospheric Sciences, 1371 Campus Delivery, Fort Collins, CO 80523-1371, USA. E-mail: guy@atmos.colostate.edu

Ground-based radar observations at three distinct geographical locations in West Africa along a common latitudinal band (Niamey, Niger (continental), Kawsara, Senegal (coastal), and Praia, Republic of Cape Verde (maritime)) are analyzed to determine convective system characteristics in each domain during a 29-day period in 2006. Ancillary datasets provided by the African Monsoon Multidisciplinary Analyses (AMMA) and NASA-AMMA (NAMMA) field campaigns are also used to place the radar observations in context. Results show that the total precipitation is dominated by propagating mesoscale convective systems. Convective characteristics vary according to environmental properties, such as vertical shear, CAPE, and the degree of synoptic forcing. Data are bifurcated based on the presence or absence of African easterly waves. In general, African easterly waves appear to enhance mesoscale convective system strength characteristics (e.g. total precipitation and vertical reflectivity profiles) at the inland and maritime sites. The wave regime also resulted in an increased population of the largest observed mesoscale convective systems observed near the coast, which led to an increase in stratiform precipitation. Despite this increase, differentiation of convective strength characteristics was less obvious between wave and no-wave regimes at the coast. Owing to the propagating nature of these advecting mesoscale convective systems, interaction with the regional thermodynamic and dynamic environment appears to result in more variability than enhancements due to the wave regime, independent of location. Copyright © 2011 Royal Meteorological Society

Key Words: mesoscale convective system; African easterly wave; West African monsoon; convective and stratiform precipitation; regional precipitation

Received 24 January 2011; Revised 5 April 2011; Accepted 7 April 2011; Published online in Wiley Online Library 8 June 2011

Citation: Guy N, Rutledge SA, Cifelli R. 2011. Radar characteristics of continental, coastal, and maritime convection observed during AMMA/NAMMA. *Q. J. R. Meteorol. Soc.* **137**: 1241–1256. DOI:10.1002/qj.839

1. Introduction

The West African monsoon (WAM) is characterized by the northward migration of the intertropical convergence zone (ITCZ), which reaches the furthest northward extent in August (Hastenrath, 1991). The Sahel is among the northernmost regions affected by the encroaching moisture, receiving over 80% of its annual rainfall in boreal summer (Laurent *et al.*, 1998; Mathon *et al.*, 2002). Mesoscale convective systems (MCSs) are primary contributors of rainfall totals in West Africa (Le Barbé and Lebel, 1997; D'Amato and Lebel, 1998; Laurent *et al.*, 1998; Mathon *et al.*, 2002; Redelsperger *et al.*, 2002; Fink *et al.*, 2006), despite their small contribution to convective system

population numbers (Mohr *et al.*, 1999). Highly organized continental MCSs often take the form of squall lines (SLs) (Hamilton *et al.*, 1945; Eldridge, 1957; Bolton, 1984; Houze *et al.*, 1989), while systems in the adjacent east Atlantic region are often more stratiform in nature (Schumacher and Houze, 2003, 2006; Fuentes *et al.*, 2008), with a transitional region for systems exiting the West African coast (Sall and Sauvageot, 2005; DeLonge *et al.*, 2010).

A key feature of the WAM are African easterly waves (AEWs), which have periods of 3–5 days (Carlson, 1969a; Burpee, 1972; Reed *et al.*, 1977; Diedhiou *et al.*, 1999), with wavelengths near 3000 km and mean speed of approximately 8 m s^{-1}. Cyclonic vortices (wave troughs) propagate westward along two tracks, one south and one north of the African easterly jet (AEJ), displaying a mixed barotropic–baroclinic growth mechanism. Hsieh and Cook (2005) showed that AEW generation may be correlated with convection within the ITCZ. More recently, Thorncroft *et al.* (2008) suggested that upstream MCSs may provide the initial perturbation into the jet entrance required for AEW generation.

Favourable large-scale dynamical forcing for the generation of rainfall through the organization of MCSs may be provided by AEWs. For example, Fink and Reiner (2003) indicated that 40% of SLs in West Africa were forced by AEWs; and Taleb and Druyan (2003) reported that 30–40% of total rainfall recorded at stations in West Africa from 1953 to 1978 was associated with AEWs. A number of previous studies, based upon satellite and reanalysis data, have reported the effects of AEWs on the modulation of precipitation (Burpee, 1974; Carlson, 1969a; Duvel, 1990; Diedhiou *et al.*, 1999; Mathon *et al.*, 2002; Fink and Reiner, 2003; Gu *et al.*, 2004; Mekonnen *et al.*, 2006), with latitudinal phasing dependence. Debate remains as to the phasing of deep convection in West Africa with AEWs, with deep convection occurring ahead of, within, or behind the AEW trough (Diedhiou *et al.*, 1999; Fink and Reiner, 2003; Kiladis *et al.*, 2006; Laing *et al.*, 2008; Payne and McGarry, 1977). These studies suggest synoptic-scale characteristic modulation, as opposed to mesoscale modulation (i.e. MCS characteristics) discussed in this study.

African MCS lifetimes have been reported as between 2 and 3 hours (Chong *et al.*, 1987) and greater than 2 days (Fink *et al.*, 2006), though it is quite possible that extremely long lifetimes could be a function of convective regeneration. Fortune (1980) and Peters and Tetzlaff (1988) observed that Sahelian SLs can move faster than AEWs with propagation speeds that average between 14 and 17 m s^{-1} (Aspliden *et al.*, 1976). Fink *et al.* (2006) found median values largely between 3 and 19 m s^{-1}, dependent upon intensity metrics used. These observed MCS speeds indicate that propagation into or through multiple phases of an AEW synoptic environment is possible, which suggests complex spatial-scale interactions between AEWs and MCSs during the WAM season.

There have been numerous case studies involving ground-based radar data (Houze and Cheng, 1977; Chong *et al.*, 1987; Barthe *et al.*, 2010), along with Doppler velocity analyses (Roux, 1988; Roux and Ju, 1990; Chong, 2009) of individual African convective events. Previous studies have also examined convective characteristics for small (Buarque and Sauvageot, 1997; Shinoda *et al.*, 1999; Fink *et al.*, 2006) and large (Geerts and Dejene, 2005; Fuentes *et al.*, 2008; Laing *et al.*, 2008) spatial regions over West Africa. These studies focused on the timing and magnitude of precipitation along with general convective characteristics, but did not emphasize the comparison of mesoscale characteristics at different locations. The sites in this study are located in unique geographical (continental, coastal, and maritime) locations along a common latitudinal band near a transitional zone in the WAM, marked by the northward extent of monsoon moisture from the south.

The objective of this study is twofold. First, we compare MCS statistics including precipitation and vertical structure for three distinct locations in West Africa. This study benefits from the African Monsoon Multidisciplinary Analysis (AMMA; Redelsperger *et al.*, 2006; Lebel *et al.*, 2010) and the NASA-AMMA (NAMMA; Zipser *et al.*, 2009) experiments, which allowed access to a great deal of observational data in what is normally a sparsely observed area of the globe. The temporal extent of the study was determined by the common operating period (19 August–16 September 2006, Table I) of the three ground-based radars. Secondly, differences in convective characteristics between MCSs associated with AEWs and those that are not are explored for each radar location.

2. Data and methodology

2.1. *Radar data and precipitation feature analysis*

Data and methodologies largely follow Cifelli *et al.* (2010), with additions elaborated hereafter. Radar data were the primary datasets for the analysis of convective characteristics. Figure 1 shows the location of each radar site and the approximate maximum unambiguous range about each radar location. The continental (Massachusetts Institute of Technology, MIT) and maritime (Tropical Ocean and Global Atmosphere, TOGA) radar systems were both C-band, single polarimetric, while the coastal radar system (NASA Polarimetric Radar; NPOL) operated at S-band with dual polarimetric capabilities. The NPOL dual polarimetric information was not used in this study. Sampling characteristics, along with the location of each radar system, are listed in Table I. Quality control was performed on each dataset to remove spurious echoes. In addition to internal calibrations performed in the field, calibration comparisons of radar reflectivity against the TRMM precipitation radar (TRMM PR) were performed following methodologies described in Anagnostou *et al.* (2001) and Lang *et al.* (2009). Adjustment values are shown in Table II. The attenuation correction algorithm of Patterson *et al.* (1979) was applied to both C-band radar systems.

Radar polar coordinate data were interpolated to a 2 km vertical and horizontal resolution Cartesian grid using the National Center for Atmospheric Research REORDER software (Mohr *et al.*, 1986). The grid extended 130 km in the x and y directions from the radar location listed in Table I. The spacing chosen was a direct result of different sampling characteristics (Table I), so data interpolated to the Cartesian grid did not exceed maximum spatial resolution of any dataset at the maximum unambiguous range.

Radar reflectivity (Z) volume scans were partitioned into convective and stratiform components using the Steiner *et al.* (1995) algorithm. This technique uses a convective threshold value to identify convective cores, along with a convective peakedness criterion which evaluates surrounding pixels for convective classification. Rainfall (R) estimates

Table I. Sampling characteristics and locations of TOGA, NPOL, and MIT radars.

	TOGA (maritime) Praia, Cape Verde	NPOL (coastal) Kawsara, Senegal	MIT (continental) Niamey, Niger
3 dB beamwidth (°)	1.66	1.00	1.40
Pulse repetition frequency (Hz)	1001	950	950
Repeat cycle (min)	10	15	10
Wavelength (m)	0.053	0.107	0.053
Range gate size (m)	150	200	250
Unambiguous range (km)	150	157	158
Pulse width (μs)	0.8	0.8	1.0
Latitude location	14.92°N	14.66°N	13.49°N
Longitude location	23.48°W	17.10°W	2.17°E
Period of operation, 2006	15 Aug–16 Sep	19 Aug–30 Sep	5 Jul–27 Sep

Table II. Data and methodology characteristics for TOGA, NPOL, and MIT radars.

Location	Radar reflectivity adjustment via TRMM comparison (dB)	Z–R relationship	Partial features (%)
Maritime (TOGA)	−3.6	$Z = 230R^{1.25}$	34
Coastal (NPOL)	+2.0	$Z = 368R^{1.24}$	18
Continental (MIT)	+0.0	$Z = 364R^{1.36}$	52

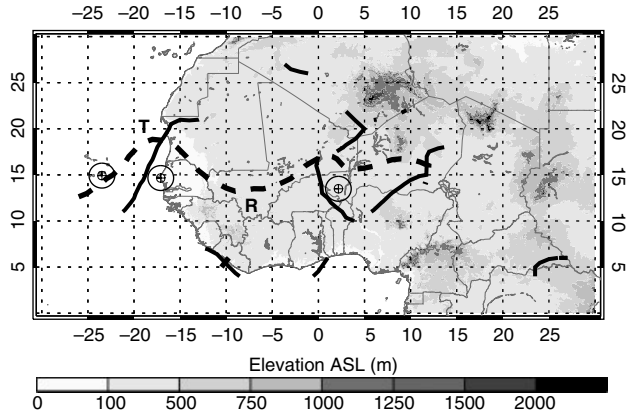

Figure 1. Map of West Africa with shaded topography. The three radar systems are located at the crosshairs, with the encircled regions showing the approximate observational scan range. Objectively identified AEJ axis (dashed line) and AEW troughs (solid lines) are shown for 8 September 2006 at 1200 UTC, with trough ('T') and ridge ('R') positions labeled.

were made from power-based Z (in mm^6 m^{-3})–R (in mm h^{-1}) relationships (Table II). The relations chosen were based upon radar–rain gauge comparisons for the GARP Atlantic Tropical Experiment (GATE) region (Hudlow, 1979) for TOGA; and disdrometer data in Dakar (Nzeukou *et al.*, 2004) for NPOL and Niamey (Sauvageot and Lacaux, 1995) for MIT. The TOGA relationship produced a higher rainfall rate for the same Z value when compared to the corresponding Z–Rs used for NPOL and MIT, consistent with previous Z–R relationships for oceanic regimes. A single Z–R relation was used for both convective and stratiform portions at each location. As with any precipitation estimator, there is inherent error associated with the use of Z–R relations.

Divergence profiles were calculated using the method described by Mapes and Lin (2005), which is a refined derivative of the Browning and Wexler (1968) velocity azimuth display (VAD) method. Briefly, polar-coordinate radar data were processed via a space–time binning algorithm (CYLBIN) to retain range-dependent characteristics. Data were pooled into 50 hPa vertical levels to account for sparse data at upper levels, while 8 km annuli were used in horizontal processing over ranges of 4–92 km. Methodology for attaining mean divergence profiles follows Hopper and Schumacher (2009), in which 40 km annuli (five-range pooling) centered about 28, 44, 60, and 76 km were used.

Ground-based radar observations in this study do not allow examination of the evolution and structural differences of the largest MCSs, due to both geographic position and limited observational domains. The spatial extent of MCSs may be several times larger than the radar scan domain and Hodges and Thorncroft (1997) showed that MCSs are preferentially generated >5° from the most eastward radar location. Despite these limitations, ground-based observations allow detailed analysis of a smaller subset of convective systems. In order to analyze convective characteristics of radar data, precipitation features (PFs) were identified using an objective algorithm described in Cifelli *et al.* (2007), related to an approach developed for TRMM satellite observations (Nesbitt *et al.*, 2000, 2006). A contiguous echo region that meets a minimum threshold reflectivity (10 dBZ) and size criterion (8 km or 4 pixels in this case) was identified in the lowest grid level (1 km AGL). The algorithm then broke these into three categories: MCS ($\geqslant$1000 km^2, with at least one convective grid point), sub-MCS (<1000 km^2, with at least one convective grid point), and no convective (NC; features that did not display required convective criteria regardless of spatial scale). Statistics of associated precipitation, reflectivity, vertical structure, and number of elements were recorded for each feature. In addition, representative thermodynamic variables (discussed later) were retained.

While ground-based radar data provide high spatial and temporal resolution, it is important to note the limitation of the radar scan area. Owing to the high frequency of large convective systems extending beyond the scan range of the radar, it is impossible to completely sample the largest convective systems within the view area of a single

radar system (confirmed through infrared (IR) satellite animations; not shown). Buarque and Sauvageot (1997), using radar and rain gauge data from Niamey, suggested that rainfall estimates may scale radar estimates, dependent upon the mode of convection (i.e. SL, convective line, stratiform region) for an area calculation technique. Nesbitt *et al.* (2006) showed that feature area is comparable for continental and ocean systems, though the continental site did display overall larger system size in West Africa (confirmed in the present study). In this study, the continental site exhibited the largest fraction of partial features (features that occur at the edge of the scan region and were not fully sampled; Table II). Further analysis showed that partial features contributed similar fractions of rain volume and feature area at all sites. Because the emphasis of this study is on understanding the relative trends in the statistics, the occurrence of partial features should not adversely affect the analysis.

2.2. Radiosonde data

Radiosonde data collected near each radar location (Praia (TOGA), Kawsara/Dakar (NPOL), and Niamey (MIT)) have undergone extensive quality control and corrections (Nuret *et al.*, 2008; Agustí-Panareda *et al.*, 2009). Sounding launch intervals were approximately 4 hours (0000, 0400, 0800, 1200, 1600, 2000 UTC) at Praia, roughly 6 hours (0000, 0600, 1200, 1800 UTC) at Niamey and Kawsara, and twice daily (0000, 1200 UTC) at Dakar. Missing data at Kawsara reduced the number of usable soundings. Inspection of time series and variable distributions showed that Kawsara and Dakar soundings were nearly the same, therefore, given their close proximity (approximately 40 km); these two datasets were combined to improve temporal resolution. A number of thermodynamic characteristics were calculated for each sounding to characterize local environments for convective generation conditions, including convective available potential energy (CAPE), convective inhibition (CIN), and low-level shear (surface to low-level maximum zonal wind). Pseudo-adiabatic parcel ascent from mixed layer (bottom 50 hPa of sounding) was used in CAPE and CIN calculations. The methodology of Lucas *et al.* (2000) was used for the shear calculations. Time series correlations were tested using rank and product–moment correlations. The Wilcoxon–Mann–Whitney hypothesis test was applied at the 95% significance level for non-normal data distributions (i.e. CAPE), which is a nonparametric rank method that tests whether two samples are from the same or different populations.

2.3. Reanalysis data and easterly wave analysis

The NASA Goddard Space Flight Center (GSFC) Global Modeling and Assimilation Office (GMAO) Modern Era Retrospective analysis for Research and Applications (MERRA) product (Bosilovich *et al.*, 2006), based upon the Goddard Earth Observing System Version 5 (GEOS-5) general circulation model (Rienecker *et al.*, 2008), was used for identifying AEWs during the 2006 season.

Wave identification was performed using 700 hPa winds and the methodology discussed by Berry *et al.* (2007), in which the westward advection of curvature vorticity is employed for trough tracking. This algorithm is one of the few that explicitly attempts to reduce noise associated with the vorticity field from individual MCSs through the elimination of divergent flow. Results using the native resolution (0.5° latitudinal × 0.67° longitudinal) resulted in a discontinuous vorticity field between time steps. By degrading the reanalysis product to a 1° × 1° grid, the algorithm produced a cleaner vorticity field in which trough tracking was easily attained. Wave identification results using MERRA were found to be comparable to those produced by the European Centre for medium-range weather forecasts interim reanalysis (not shown). An example of an objectively identified AEJ axis (dashed line) and AEW troughs (solid lines) are shown in Figure 1.

Owing to previous association of precipitation and AEW troughs, it was of interest to analyze convective characteristics while in the presence of an AEW (wave regime) and while no AEW was present (no-wave regime). To accomplish this, systems occurring within 500 km of an AEW trough identified in the MERRA dataset were assumed to be associated with the wave regime (approximately a mean AEW wavelength). Previous research has shown that triggering and maintenance of convection occurs at this scale (Berry, 2009), including the top 10th percentile of intense convective events (Nicholls and Mohr, 2010).

3. Results

3.1. Study area and environmental characteristics

The 2006 July–September (JAS) season was found to have small precipitation anomalies (less than 5%) from climatological values at each location using TRMM 3B42 gridded precipitation data. A time–longitude diagram using data from 2006 averaged over 12–17°N is shown in Figure 2. Data below 12°N (southern humid region in continental Africa) may skew regional analyses via the introduction of an area with less variability (Mohr *et al.*, 2009), and was therefore excluded. The depiction of precipitation fraction data allows the cycle of convective decay and regeneration to be observed as a function of system propagation. Streaks of variable precipitation were observed, corresponding to westward propagating PFs – similar to outgoing longwave radiation diagrams (Laing *et al.*, 2008; Cifelli *et al.*, 2010). More than 10 advecting (or propagating) modes are evident in Figure 2, with varying life cycles in terms of precipitation intensities, duration, and phase speed. Objectively identified AEW trough tracks are overlaid (solid black lines). Ten AEW troughs were associated with the continental site, eight with the coastal site and 12 with the maritime site. Propagating modes averaged a speed of 14.9 m s^{-1}, while mean AEW speed was 8.5 m s^{-1}. In some cases, westward propagating precipitation events were evident along AEW trough tracks, while other trough regimes were void of precipitation. It is possible that variations in thermodynamic conditions and topography could have driven precipitation irregularity observed in the propagating modes (Laing *et al.*, 2008).

Focusing on the radar locations, time series of radar reflectivity-estimated precipitation, CAPE, and CIN are shown for the continental (Figure 3), coastal (Figure 4), and maritime (Figure 5) locations, with AEW trough passages superimposed (hatched shading). Precipitation events of long duration and large spatial coverage were generally represented by unconditional rain rates (mean over entire scan domain) greater than 0.5 mm h^{-1}. Continental convective systems were linear in organization and faster

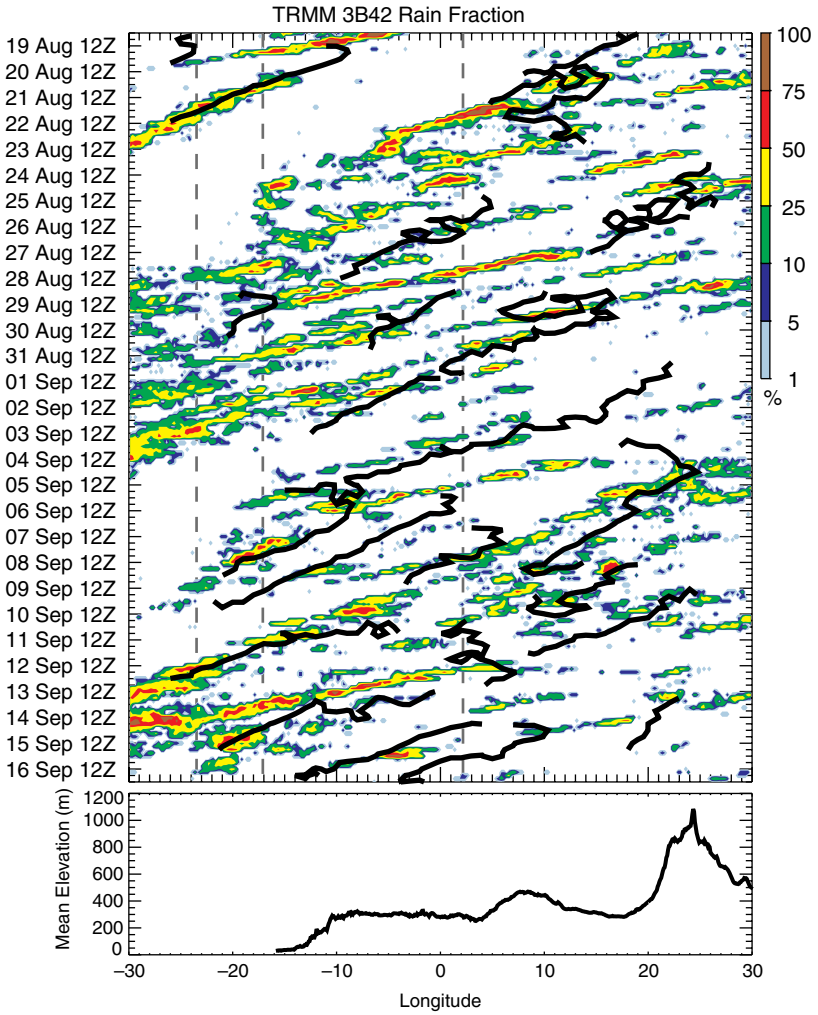

Figure 2. Time–longitude plot of TRMM 3B42 gridded rainfall product averaged between 12 and 17°N. Contours represent percentage of rainfall above threshold value (0.8 mm h^{-1}, mean value during 2006 season), with greater values representing increased areas of rain rates in observed systems – a proxy for size of precipitating system. Exclusion of data below 12°N was used to reduce 'noise' present from the southern track of precipitation associated with the summer monsoon. Objectively identified AEW trough tracks are overlaid (black lines), with all tracks that persist for less than 1.5 days and 8° in longitudinal length filtered out. Vertical, dashed lines show the location of each radar system in the study. The bottom plot denotes mean elevation between 12 and 17°N.

moving than those found over the east Atlantic (Laing and Fritsch, 1993; Hodges and Thorncroft, 1997) resulting in narrower peaks inland.

Time series of maritime CAPE in Figure 5(b) showed more variability than one might expect, likely because soundings were launched from an island large enough for nocturnal surface cooling to help establish a low-level inversion prior to daytime heating. Small values of CIN were prevalent at the coast, with greater variability at the continental and maritime sites. The largest values of CIN were observed with more frequency at the continental site. No significant correlations or anti-correlations (including lag correlation) were found between time series at each radar location. Spectral analysis of the time series showed no common precipitation or environmental periodicities between variables plotted in Figures 3–5, suggesting little dependence upon wave-driven dynamics. However, AEW and no-wave regime environmental variable populations were shown to be significantly different (discussed later).

More frequent occurrence of MCSs ahead of AEW troughs at the continental and maritime sites (60%) and an even distribution ahead and behind the trough at the coastal location were observed, in agreement with earlier studies (Carlson, 1969b; Payne and McGarry, 1977; Duvel, 1990; Machado *et al.*, 1993; Diedhiou *et al.*, 1999; Kiladis *et al.*, 2006). During MCS events at each radar site, the AEJ was predominantly located north of the radar, which agrees with observations from Mohr and Thorncroft (2006), who found that the most intense convective systems occurred south of the jet axis in September.

Interpretation of PF results was dependent upon understanding the environment within which convection occurs. Mohr and Thorncroft (2006) showed that environments of high shear and high CAPE can result in a high probability of the most intense convective systems (SLs) in West Africa, in agreement with simulations (Weisman and Klemp, 1982). Vertical wind shear is an essential component to linearly organized convective systems (Bluestein and Jain, 1985; Weisman *et al.*, 1988; Coniglio *et al.*, 2006). Nicholls and Mohr (2010) found that the top 10th percentile West African convective systems exhibited significantly stronger low-level shear. Though MCSs exist in environments with a wide range of shear, organization and system strength tend to increase with increasing shear (also true in this study despite low correlation values). Figure 6 depicts the relative frequency of CAPE (top row), CIN (middle row), and low-level shear magnitudes (bottom row) at each site.

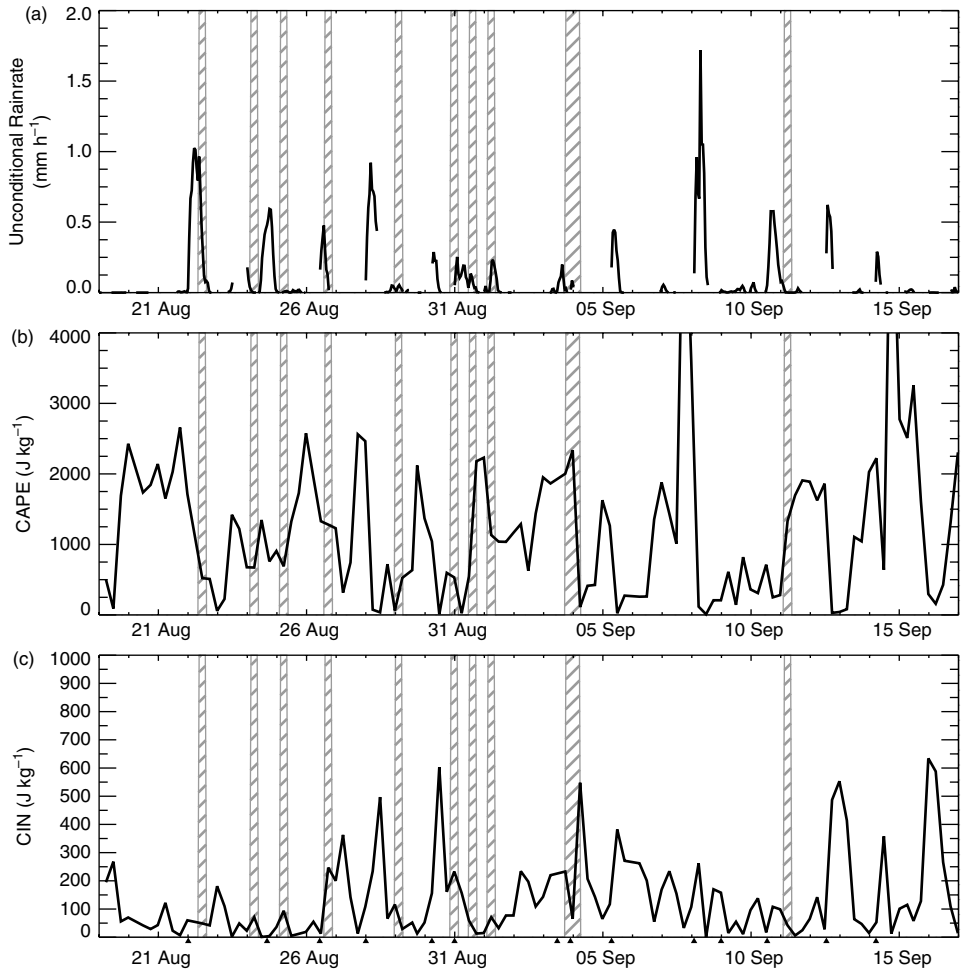

Figure 3. Time series of (a) radar-estimated unconditional rainfall rate, (b) CAPE, and (c) CIN for the continental location, 19 August–16 September 2006. Hatched, vertical bars indicate the presence of AEW troughs within 500 km of the site. Arrow heads along the CIN plot abscissa indicate the first radar echo occurrence of mesoscale convective systems of large spatial (>1000 km^2) and temporal (>3 h) extent.

The distribution of CAPE at the maritime location (Figure 6(a); 1090 J kg^{-1} median value) was skewed toward lower values, while the coastal location displayed a tendency toward larger CAPE values (Figure 6(d); 1842 J kg^{-1} median value). The continental site (Figure 6(f); 1044 J kg^{-1} median value) was centered about more moderate CAPE values; though extremely large quantities up to 6000 J kg^{-1} were observed (not shown), but confined to less than 1% of cases. Extreme CAPE values at the continental site were mostly unrealized, occurring in unfavourable conditions for convection (e.g. lack of synoptic-scale convergence, very little vertical shear, and large CIN). The continental domain exhibited a 50% larger CAPE value during AEW regimes (found to be significant to the 95% confidence level), while the coastal and maritime locations remained nearly unchanged between wave and no-wave regimes. Median values and distributions of CAPE are generally consistent with Fink *et al.* (2006) and Nicholls and Mohr (2010).

Distributions skewed toward small CIN values were observed at each location. Maritime and continental values (Figure 6(b) and (h)) showed occasional large CIN, with tails extending beyond 400 J kg^{-1}, while the relative occurrence of small CIN was most frequent at the coastal site (Figure 6(e)). Occurrence fraction of sub-MCS features (fraction of time when sub-MCS convection was present) at the coastal site was 23%, while it was only 16% at the continental site, indicating that smaller CIN at the coastal site may have allowed for a higher relative occurrence of sub-MCS systems. Convective storms able to overcome the larger convective cap (shown by larger CIN values) inland resulted in more 'intense' convection in terms of vertical growth and reflectivity statistics (shown later) and is consistent with Nicholls and Mohr (2010), who found both larger CAPE and CIN values were present during intense events when compared to less-intense occurrences.

Similar median low-level wind shear values were observed for the maritime (easterly 3.7×10^{-3} s^{-1}), coastal (easterly 4.1×10^{-3} s^{-1}), and continental (easterly 4.1×10^{-3} s^{-1}) locations; however, distributions differ for each location. Mean vertical wind profiles in Figure 7 show the presence of the AEJ near 650 hPa, and a westerly low-level jet (LLJ) near the surface for both the continental and coastal sites. This configuration is consistent with the higher frequency of larger easterly shear values at these locations. Southwesterly flow at the surface gives way to easterly flow aloft inland. At the coast, mean southwesterlies were overlaid by northeasterlies up to the AEJ level. The largest difference between the AEW and no-wave regime wind profiles occurs at the coast, where a difference of approximately 3 m s^{-1} existed throughout the profile. In addition, the westerly LLJ was more pronounced during the no-wave regime. Calculations of shear from the surface to the westerly LLJ (not shown) revealed that the coastal site exhibited larger mixing potential at low levels during wave

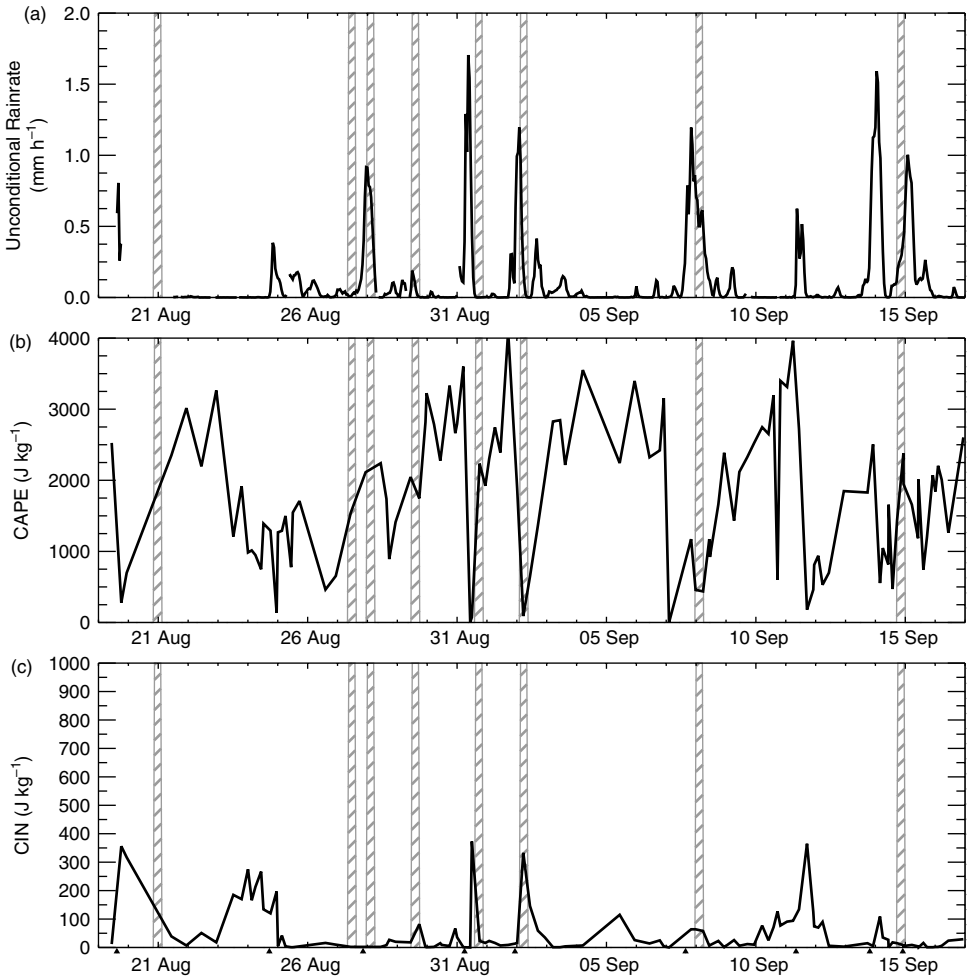

Figure 4. As Figure 3, but for the coastal location.

passage. Despite prominent changes in environmental wind profiles between AEW and no-wave regimes, the coastal location exhibited the smallest inter-regime changes in precipitation and convective characteristics in the study (shown later). Along with the relative homogeneity of CAPE mentioned earlier, this suggests that when favourable large-scale dynamics are absent, MCSs at the coastal location draw upon buoyancy to maintain their intensity, despite less environmental shear.

Mean VAD divergence profiles (Figure 8) may be used to assess the effect of MCSs on the large-scale environment. Convective cells are characterized by convergence at the surface and divergence aloft, while stratiform regions display divergence at the surface, midlevel convergence and divergence aloft (Gamache and Houze, 1982; Mapes and Houze, 1993a). Standard deviation associated with the profiles was too large to yield significant differences between the AEW and no-wave regimes. The maritime profile (Figure 8(a)) exhibited the same structure as the intermediary case (a system during the conversion process from being convective to stratiform in nature) discussed in Mapes and Houze (1993b), also for an oceanic profile. The coastal profile (Figure 8(b)) showed divergence near the surface, mid-level convergence, and divergence aloft. The continental site exhibited the same general pattern (Figure 8(c)), with decreased divergence at the surface and peak convergence occurring lower in the atmosphere. This suggests distinct heating profiles for each location. It should be noted that these profiles could be driven by time-of-arrival of propagating MCSs that were often in a similar stage of development (see section 3.3).

3.2. *Precipitation characteristics*

Table III lists statistics derived from PF analysis for the study time period, along with the statistics for both AEW and no-wave regimes. Less than 4% of total scans over the continent and even less over the coastal and maritime locations contained MCS events. Even though MCSs where infrequent, MCS rain volume fractions (of total observed precipitation) were large, in line with previous studies using IR (80–90%; Mathon and Laurent, 2001) and TRMM microwave satellite data (60–80%; Mohr *et al.*, 1999; Nesbitt *et al.*, 2006), with a mean Sahelian value near 80% of annual precipitation.

A marked decrease at successive westward locations is observed in MCS area fractions (echo area coverage contributed by MCS-scale features; Table III). The percentage of area covered by continental and coastal MCSs was larger than sub-MCSs, while maritime MCSs and sub-MCSs covered an equivalent percentage of area, which agrees with Liu *et al.* (2008), who showed that the population of large satellite-observed systems decreased from West Africa into the East Atlantic at this latitude.

Contrary to results from previous studies, the stratiform precipitation fraction increased from west to east. Stratiform

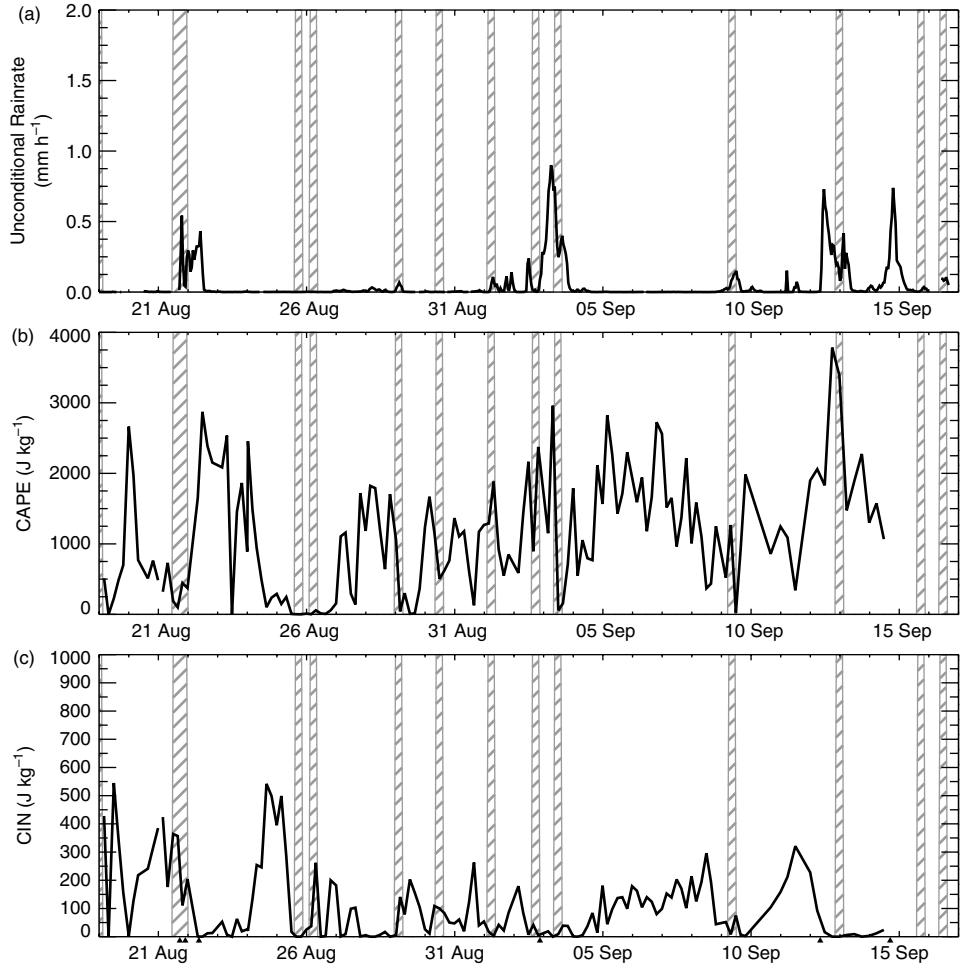

Figure 5. As Figure 3, but for the maritime location.

Table III. Convective system characteristics derived from precipitation feature analysis for all study times and within AEW and no-wave regimes.

Location	Regime	MCS occurrence fraction (%)	MCS rain volume fraction (%)	MCS area fraction (%)	Convective (stratiform) rain volume fraction (%)	Convective (stratiform) area fraction (%)	Number of precipitation features identified
Maritime	All	0.6	83	53	64 (36)	9 (91)	14 661
(TOGA)	AEW	0.3	81	57	61 (39)	9 (91)	6 622
	No wave	0.4	73	47	66 (34)	9 (91)	8 039
Coastal	All	1.4	85	72	63 (37)	17 (83)	9 507
(NPOL)	AEW	0.6	89	81	56 (44)	16 (84)	3 031
	No wave	0.9	81	65	68 (32)	18 (82)	6 476
Continental	All	3.6	92	83	51 (49)	12 (88)	6 468
(MIT)	AEW	2.0	95	88	53 (47)	12 (88)	2 620
	No wave	1.9	88	79	49 (51)	12 (88)	3 848

precipitation fractions for the maritime (36%) and coastal (37%) regions generally agree with Schumacher and Houze (2006), while the continental site (49%) was larger by nearly 10%. This difference may be explained by the fact that this study used only 1 month of data compared to 5 years in (Schumacher and Houze, 2006) and that spaceborne precipitation estimates do not account for the evaporation of precipitation in the boundary layer. Stratiform area accounts for 90% of MCS area, which may lead to underestimation from ground-based observations, which view a much smaller domain than space-borne observations and may not sample the entire MCS area. Strong, easterly low-level shear in this region produced leading convective line, trailing stratiform MCSs that greatly affected boundary layer properties. Boundary layer relative humidity (not shown) increases an average of 5% (>20% in some cases) with the passage of the convective line of these MCSs (denoted by arrow heads along the

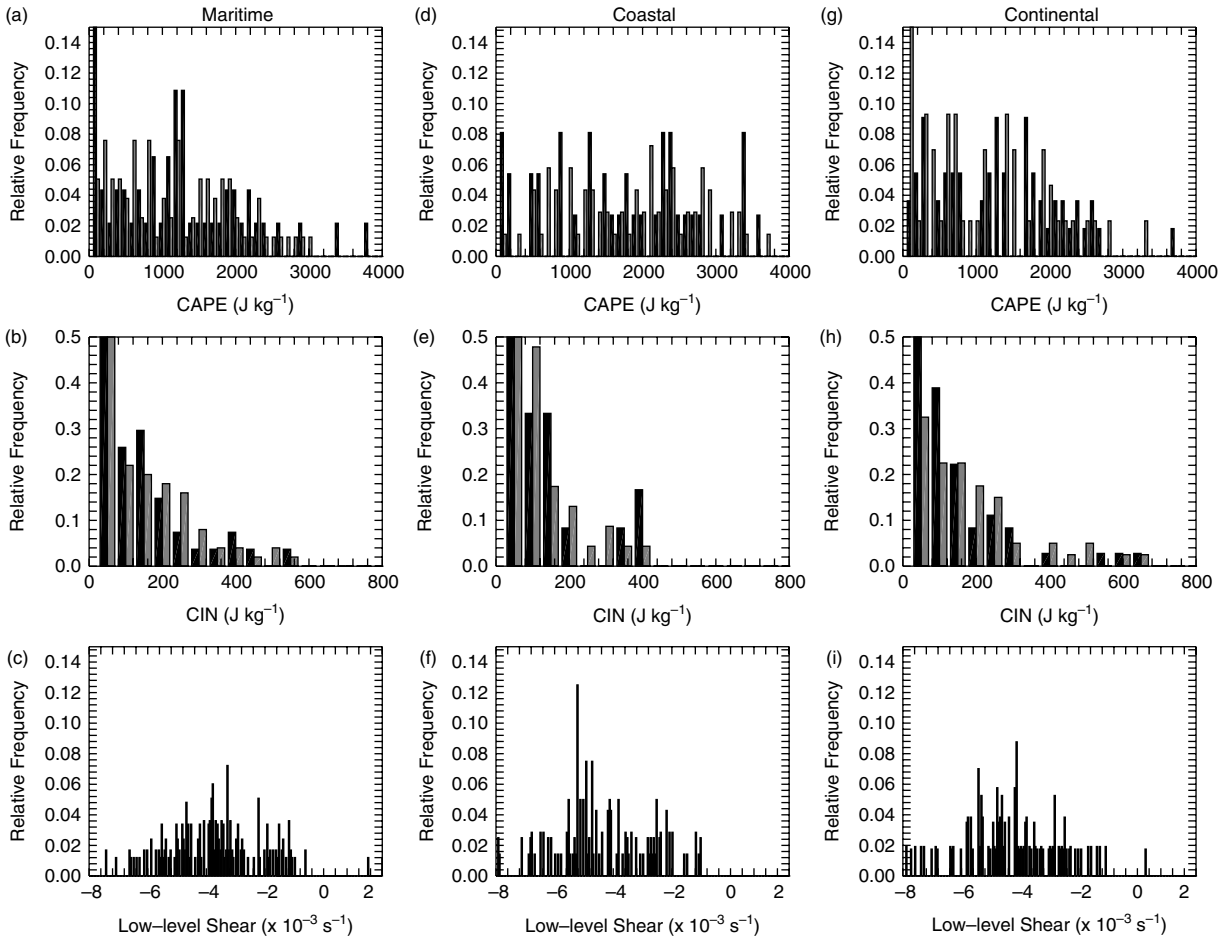

Figure 6. Frequency distribution of calculated environmental variables for the maritime (a–c), coastal (d–f), and continental (g–i) locations. CAPE (top row), CIN (middle row), and low-level shear (bottom row) are shown. Black bars represent values calculated during an AEW regime, while gray bars denote no-wave regime calculations.

bottom abscissa in Figure 3), thereby retarding evaporation of the following stratiform precipitation and increasing observed stratiform precipitation fraction. Generally, upper-level humidity increases via transport by strong convective updrafts were observed during periods of high precipitation.

To further investigate precipitation in terms of vertical structure, precipitation contributions as a function of two characteristic reflectivity levels were calculated at each vertical level. First, 20 dBZ (Figure 9(a)–(c)) echo top heights were chosen to closely match the minimum threshold of the TRMM PR and minimize contamination from spurious echo missed in the radar QC process. Second, 30 dBZ (Figure 9(d)–(f)) echo top heights were chosen to identify intense convective cells with significant mixed-phase processes (DeMott and Rutledge, 1998). Data for all occurrences are shown; exclusion of sub-MCSs did not affect the distributions.

A strong bimodal distribution at the maritime location (9 and 15–17 km peaks), a weak bimodal distribution at the coast (9 and 15 km peaks), and a broad, unimodal distribution (15 km peak) at the continental site were seen in the 20 dBZ distributions. The maritime and coastal distributions suggest distinct modes, while the continental site appears to be influenced by a deeper spectrum of vertical development. Convective precipitation controls the contribution from the deep mode at all sites, while the stratiform precipitation occurs at a lower height. The stratiform contribution generally exhibits a more narrow vertical distribution, with the exception of the broad stratiform distribution at the continental site.

The 30 dBZ distributions indicate that the continental and coastal locations had deeper, more intense convective modes than the maritime site. The continental and coastal distributions fall off less rapidly from the 7–9 km peak, with a secondary peak in the coastal distribution near 13 km. More vertically developed storms display a greater propensity for mixed-phase processes (DeMott and Rutledge, 1998; Nesbitt *et al.*, 2006), enhancing the stratiform region and leading to larger precipitation contribution over the course of the study from deep convection observed over the continent (Figure 9(e)–(f)). DeLonge *et al.* (2010) showed that MCSs transitioning from land to ocean exhibit signs of disorganization, resulting in less intense convective characteristics over the ocean. Figure 4 indicates that storms at the coast experienced a higher likelihood to enter a region with higher CAPE, which would theoretically produce stronger updrafts and significant lofting of precipitation-sized particles. Greater low-level shear over the land could act to enhance linear organization, resulting in two distinct modes (ocean and land) of vertical development present during the study period.

It is well established that the diurnal cycle of precipitation in West Africa is largely controlled by propagating MCSs (Reed, 1978; Shinoda *et al.*, 1999; Mohr, 2004; Fink *et al.*, 2006; Laing *et al.*, 2008; McGarry and Rickenbach *et al.*, 2009) and is a function of distance from genesis and

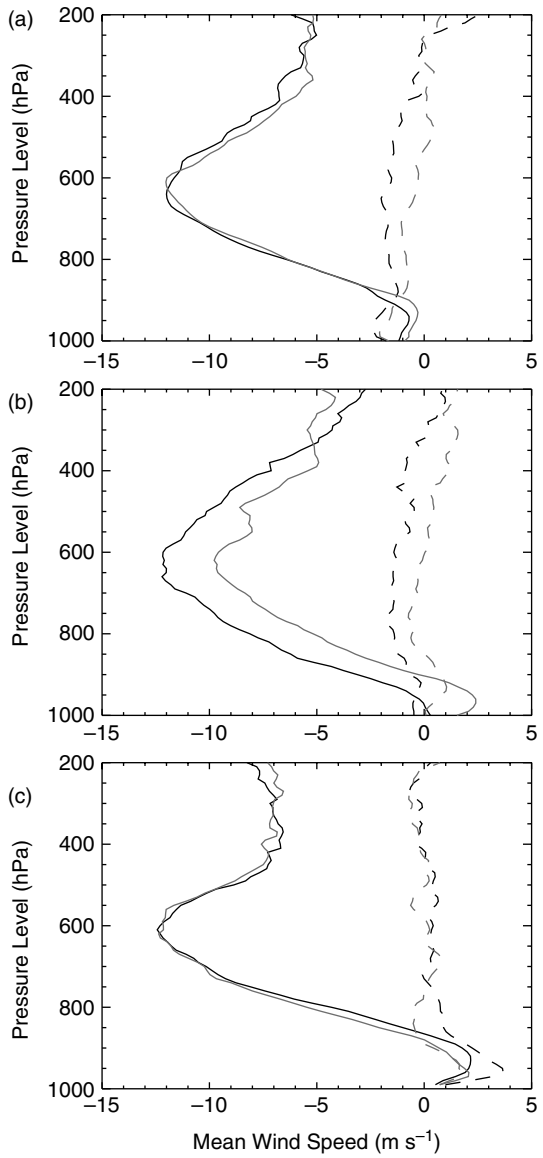

Figure 7. Mean zonal (solid lines) and meridional (dashed lines) vertical wind profiles for the (a) maritime, (b) coastal, and (c) continental locations. Mean rawinsonde profiles are shown for the African easterly wave (black) and no-wave (gray) regimes.

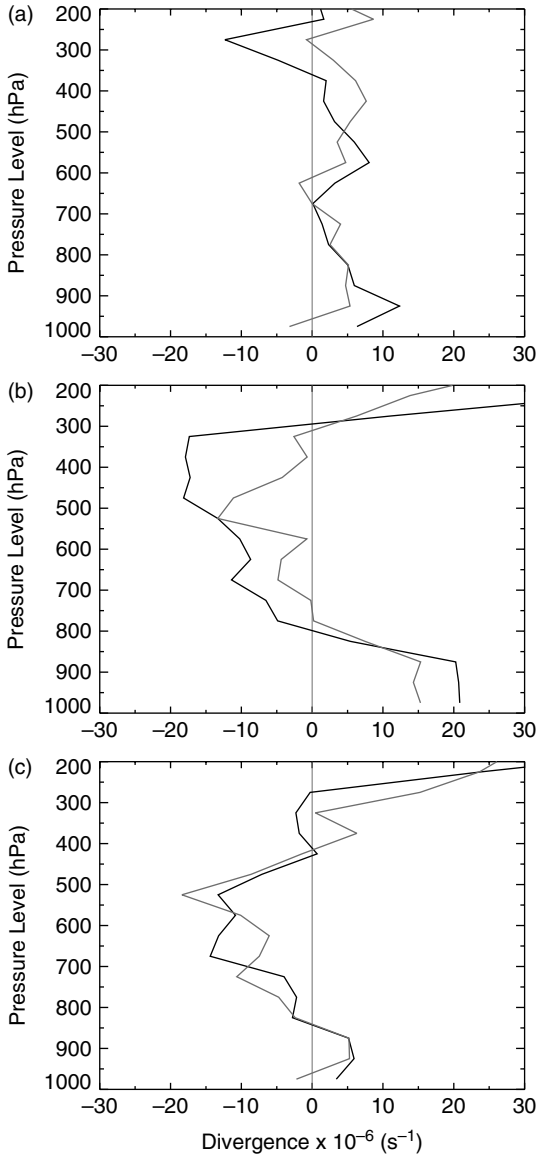

Figure 8. Mean velocity azimuth display divergence profiles for the (a) maritime, (b) coastal, and (c) continental locations. Profiles of 40 km annuli centered about ranges of 24, 44, 60, and 76 km from the radar are averaged for AEW (black) and no-wave (gray) regimes. Profiles are made up of both convective and stratiform components.

redevelopment regions (e.g. high terrain; Hodges and Thorncroft, 1997; Mohr, 2004). This pattern was confirmed in this study in conjunction with Meteosat imagery (not shown), showing peak precipitation occurring near 0800 LT at the continental site, 0200 LT at the coastal and maritime sites.

3.3. *Convective characteristics and easterly waves*

Analysis of longer time period radar-estimated precipitation at the continental site showed a peak precipitation interval every 3–4 days (Nieto Ferreira *et al.*, 2009), suggesting a correlation to AEW trough passage at this longitude. While precipitation events did occur near trough passages during the time frame of this study, many events also occurred when no wave was identified (see Table II). As a result, no significant correlation between AEWs and precipitation was noted at the continental site. Given the current debate concerning the impact of AEWs on precipitation, it was of interest to compare convective system characteristics during periods of AEW passage and periods of no AEW forcing. The intent was to take advantage of radar data from the three sites to further elucidate effects of AEW forcing on convective characteristics (i.e. vertical and horizontal structure) and to understand possible feedbacks of these mesoscale features onto the larger scale (i.e. MCS latent heat release).

Table IV lists contributions of AEW regime PFs during the study period, with 37–57% (32–45%) of total rain volume (feature area) associated with the AEW regime at all sites; less than previous results. Only the continental site showed that greater than half of the total estimated precipitation occurred during the AEW regime. Laing *et al.* (2008) found that about 80% of the deep convective area (as identified by satellite cold cloud streaks) was associated with AEWs for a region from 10°W to 10°E. The discrepancy with the current study may be attributed to differences between the PF definition used here and the classification of convection based upon minimum IR brightness temperatures. Ground-based radar observations yield a more direct picture of the spectrum of precipitating features, while IR precipitation estimates are

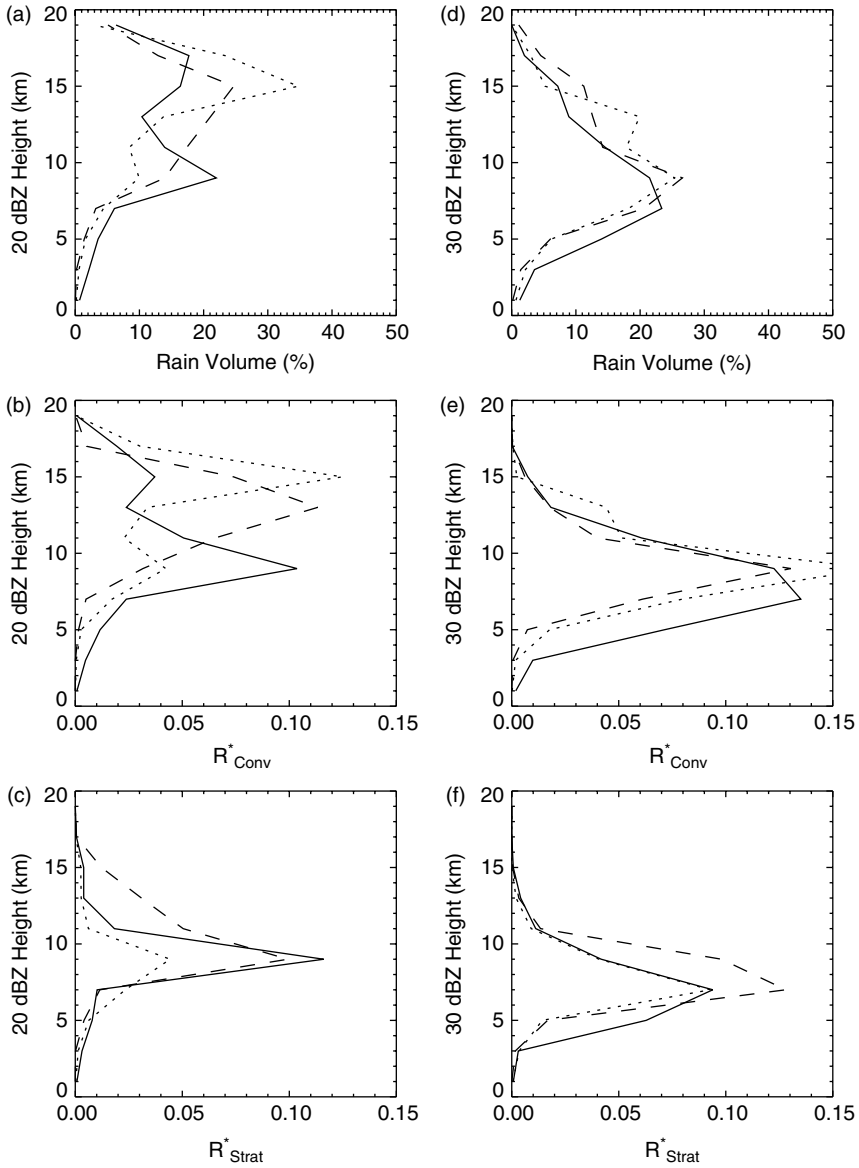

Figure 9. Contribution by precipitation features, at the maritime (solid line), coastal (dotted line) and continental (dashed line), to total volumetric rainfall as a function of mean (a–c) 20 dBZ and (d–f) 30 dBZ echo-top heights. Convective (b, e) rain volume-weighted reflectivity occurrence distributions normalized by maximum occurrence were used to illuminate the convective mode of precipitation. The same methodology was used for stratiform (c, f) contributions.

based upon persistent, high cloud shields associated with MCSs. Therefore the estimation and temporal evolution of precipitation may differ between these methodologies and result in partitioning differences.

To further consider differences during AEW and no-wave regimes, cumulative frequency distributions (CFDs) of the feature area (Figure 10(a)) and rain volume (Figure 10(b) and (c)) were created and the distribution differences ($CFD_{AEW} - CFD_{no-wave}$) analyzed. Regime populations were found to be significantly different from the 99% confidence level. The AEW regime was associated with broad increases in PF size at the continental and coastal locations, with the coastal peak increase offset to larger systems. Feature size decreased during the AEW regime at the maritime location, with a maximum decrease at the sub-MCS scale. Examination of convective and stratiform precipitation volume distributions revealed that continental convective precipitation (Figure 10(b)) was enhanced during the AEW regime, while stratiform precipitation (Figure 10(c)) decreased. Little change was observed at the coast for convective precipitation, with an increase in stratiform precipitation during the AEW regime. Convective precipitation decreased at the maritime site during the AEW, while stratiform precipitation showed little deviation between regimes. Inspection of PF distribution along with environmental variables may help clarify the differences shown in convective and stratiform precipitation.

The increase in system size and convective rain volume at the continental site (Figure 10(a)) is consistent with increased CAPE, decreased CIN, and weaker shear, resulting in a shift of sub-MCSs to MCS-scale that occurred during the AEW regime compared to the no-wave regime. Increased large system population at the coast may have been driven by increased CIN and vertical shear, which resulted in a greater thermodynamic triggering barrier and provided increased organization for larger systems at the expense of smaller systems. A reduction in CIN and weaker vertical shear in the lowest 3 km were observed during the wave regime at the maritime site, explaining the formation of weaker, smaller convection.

Table IV. Contribution of AEW regime precipitation features as a function of study period totals.

Location	Total feature fraction (%)	Total rain volume fraction (%)	Convective rain volume fraction (%)	Stratiform rain volume fraction (%)
Maritime	45	37	35	41
Coastal	37	45	41	53
Continental	41	57	59	55

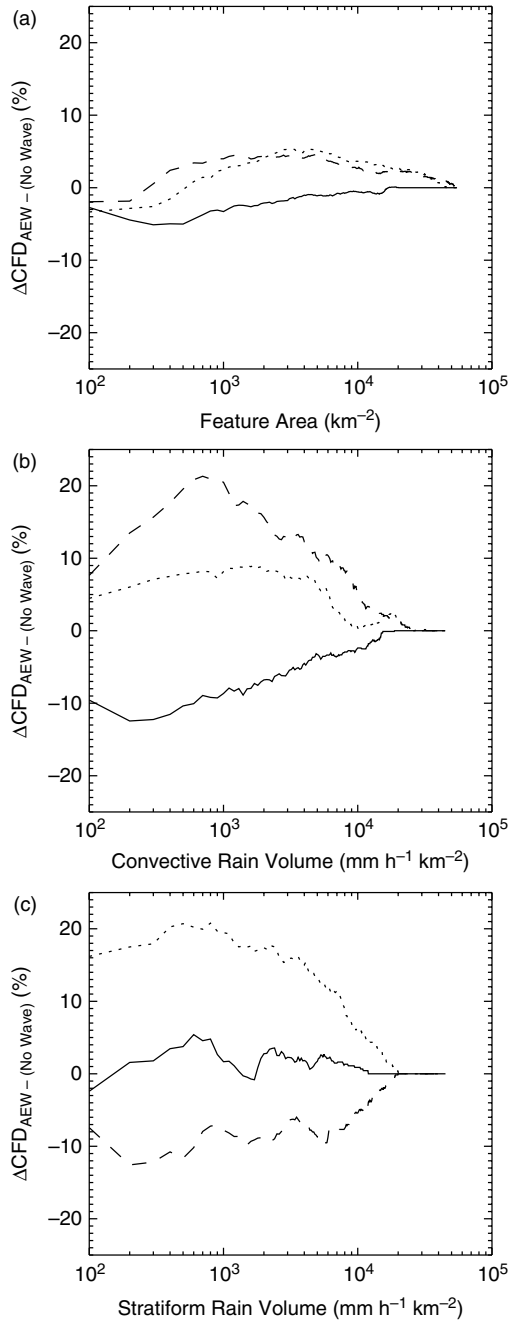

Figure 10. Difference in cumulative frequency distributions between AEW and no-wave regimes for (a) precipitation feature area, (b) convective and (c) stratiform volumetric rainfall. Maritime (solid line), coastal (dotted line), and continental (dashed line) locations are shown. Positive values correspond to an increase during the AEW regime. Less (more) volumetric rainfall may be interpreted as a decrease (increase) in precipitation rate and/or increase (decrease) in precipitation spatial coverage.

Differences in convective and stratiform contributions can be further elucidated in terms of mean vertical reflectivity profiles (Figure 11). Convective (stratiform) profiles for each site are similar, with near surface mean values of 36–40 (22–28) dBZ. The decrease in reflectivity with height is similar for all three locations. Continental and maritime AEW regime convective profiles were more intense and exhibited higher reflectivity values aloft compared to the no-wave regime, suggesting hydrometeor loading aloft due to strong updrafts. Note that the number of points was an order of magnitude less for the continental no-wave regime, also suggesting less vertical growth overall. The coastal site exhibited very little difference in convective reflectivity profiles for AEW and no-wave regimes, which agrees with convective precipitation differences noted earlier (Figure 10(b)). Land-to-ocean transitioning MCSs (coastal site) have been shown to diminish in strength (e.g. DeLonge *et al.*, 2010) due to less favourable thermodynamic (e.g. lower specific humidity) and dynamic (e.g. reduced vertical wind shear) conditions. The changes associated with this transition may have mitigated enhanced synoptic-scale moisture flux convergence and potential vorticity during the AEW regime to mediate vertical reflectivity profiles.

A brightband signature, owing to the melting of aggregates common in organized MCSs (Houze *et al.*, 1989), was observed near 3–5 km in the stratiform profile at the coastal and continental sites. Decreasing reflectivity below this level toward the surface is a signature of droplet evaporation below cloud base, consistent with mesoscale descent. The continental AEW regime stratiform profile decreased more rapidly with height when compared to the no-wave regime, consistent with the reduction in stratiform rain area (Figure 10(c)) noted earlier. The order of magnitude difference in the continental number of points profile might suggest the importance of large-scale dynamics during the AEW regime on MCSs for the maintenance of the stratiform shield at this site. The consequences of these profiles are that MCS heating profiles at the coastal and maritime locations are comparable for the wave and no-wave regimes, whereas at the continental site differences arise due to the modification of stratiform structure. Weaker upper-level stratiform signal during the AEW regime results in a reduction of heating aloft and a less top-heavy heating profile (Mapes and Houze, 1995).

4. Conclusions

A comparison of convective characteristics via ground-based radar statistics for three unique geographic locations (continental, coastal, and maritime) was presented for the peak of the 2006 WAM season. High spatial and temporal resolution ground-based radar observations were complemented by sounding locations near each radar system, allowing characterization of convective events and the thermodynamic environment in which they occurred.

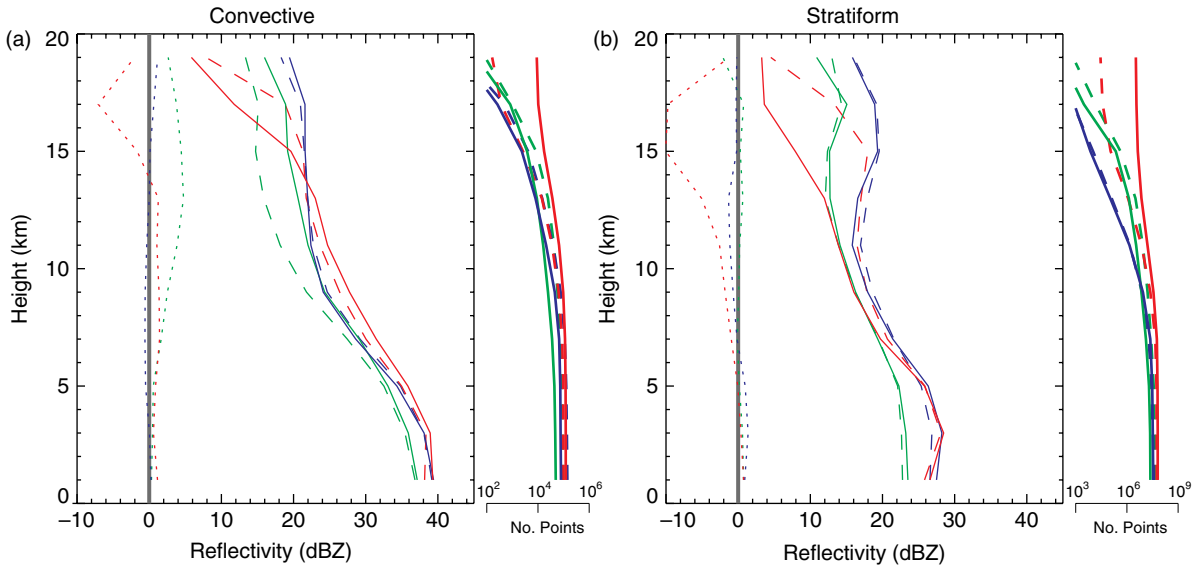

Figure 11. Vertical radar reflectivity profiles for (a) convective and (b) stratiform regimes at the maritime (green), coastal (blue), and continental (red) locations. Mean profiles for AEW passages (solid line) and no-wave (dashed line) are shown along with the difference between the AEW and no-wave regime profiles (dotted line). Secondary plots to the right of each main plot show the number of points averaged at each vertical height. Note that the order of magnitude is the same throughout the bottom 11 km.

A precipitation feature algorithm was employed to analyze precipitation and area characteristics at each site. Partitioning data in terms of convective and stratiform precipitation modes and AEW (or no-wave) presence was used to analyze geographic and regime variability of convective system structure and characteristics.

The diurnal cycle of precipitation at each location was largely dependent upon the time-of-arrival of propagating MCSs. The distribution of environmental conditions was important in determining differences in convective characteristics at each site. Key environmental and dynamical characteristics of each location are listed in Table V. All locations were generally favourable for the formation and/or maintenance of deep convection, though the extent organization, and therefore characteristics, depended upon the environment associated with each location. For example, the continental and coastal sites supported more organized, linear convection, while the maritime site exhibited less organized convective systems (important in terms of vertical growth and heating profiles of MCSs).

Phasing of MCSs with AEW troughs differed on a regional basis and precipitation was uncorrelated to trough passage during this period. The mean speed of MCS systems was greater than AEWs, suggesting a somewhat complex interaction between mesoscale and synoptic disturbances. Table VI notes the tendency of observed environmental and convective characteristics for each location during the AEW regime in comparison to the no-wave regime. The continental AEW regime displayed the greatest total precipitation, with near equal contributions from stratiform and convective components and an increase in precipitation during the AEW regime. In addition, less total precipitation was observed at the coastal and maritime locations during the AEW regime compared to the no-wave regime. Increased occurrence of large MCSs at the coast resulted in increased stratiform fraction and therefore increased stratiform precipitation. Together the results suggest important differences exist longitudinally across West Africa and to some degree whether convective systems interact with an AEW. Regional differences were generally more striking than those found between AEW and no-wave regimes at each site and were largely driven by differences in environmental characteristics.

Results presented here are limited by the short analysis period. Future work should examine climatological PFs via satellite observations, where a large number of convective systems can be sampled to better characterize differences between features associated with AEW and no-wave regimes. Timing of convection in terms of AEW passage would also be of interest to investigate systematic changes of environment by preceding convection for large systems leading to favourable feedback mechanisms with the synoptic scale (and possible cyclogenesis precursor). In addition, comparisons to inferred microphysics of different synoptic regimes and convective and stratiform components within MCSs should be compared against model simulations. Detailed study of MCS kinematics at each region would help quantify structural variability associated with geographic location and AEW and no-wave phasing, leading to a better understanding of latent heating and momentum transfer in comparison to model simulations.

Acknowledgement

This research was supported by the CEAS fellowship grant NNX08AT77G and NASA Precipitation Measurement Mission under grant NNX10AG88G. Based on a French initiative, AMMA was built by an international scientific group and is currently funded by a large number of agencies, especially from France, UK, USA, and Africa. It has been the beneficiary of a major financial contribution from the European Community's Sixth Framework Research Programme. Detailed information on scientific coordination and funding is available on the AMMA International web site http://www.amma-international.org. The NAMMA program was made possible by Dr Ramesh Kakar (NAMMA mission director). The authors would like to thank the AMMA and NAMMA project communities for maintaining

Table V. Comparison of key characteristics for each location during 19 August–16 September 2006.

	Maritime	Coastal	Continental
CAPE	Moderate	High	Moderate
CIN	Low-to-moderate	Low	Moderate
Low-level Shear	Weak-to-moderate	Moderate	Moderate-to-high
Wind profile	No LLJ	Weak LLJ	Moderate LLJ
MCS location	Ahead of AEW trough	Equal ahead and behind of AEW trough	Ahead of AEW trough
AEJ location	N of radar	N of radar	N of radar

Table VI. AEW regime characteristics in relation to no-wave regime characteristics during 19 August–16 September 2006.

		Maritime	Coastal	Continental
	AEW arrival	No preference	0000 UTC	0600 UTC
	Rain volume	−3%	+3%	+4%
Environmental	CAPE	0%	−22%	+50%
	CIN	−55%	+68%	−44%
	Low-level Shear	+1%	+31%	−3%
Precipitation Features	Area	0%	+2%	+2%
	Convective rain	−2%	+3%	+6%
	Stratiform rain	+1%	+6%	−4%
	Stratiform fraction	+5%	+12%	−4%

and distributing datasets. MIT radar data were provided by Earle Williams. NPOL radar data were provided by Paul Kucera. Sounding data at Niamey, Kawsara, Dakar, and Praia were provided by Doug Parker, Marcia DeLonge, Serge Janicot, and Francis Schmidlin, respectively. We would like to acknowledge the Global Modeling and Assimilation Office (GMAO) and the GES DISC for the dissemination of MERRA. Gareth Berry provided computer code for AEW analysis. We had important discussions with Chris Thorncroft, Ed Zipser, Arlene Laing, John Zawislak, and Tom Rickenbach. The authors would also like to thank Karen Mohr, who provided invaluable advice on this manuscript.

References

Agustí-Panareda A, Vasiljevic D, Beljaars A, Bock O, Guichard F, Nuret M, Garcia Mendez A, Andersson E, Bechtold P, Fink A, Hersbach H, Lafore J, Ngamini J, Parker DJ, Redelsperger J, Tompkins AM. 2009. Radiosonde humidity bias correction over the West African region for the special AMMA reanalysis at ECMWF. *Q. J. R. Meteorol. Soc.* **135**: 595–617.

Anagnostou EN, Morales CA, Dinku T. 2001. The use of TRMM precipitation radar observations in determining ground radar calibration biases. *J. Atmos. Oceanic Technol.* **18**: 616–628.

Aspliden C, Tourre Y, Sabine J. 1976. Some climatological aspects of West African disturbance lines during GATE. *Mon. Weather Rev.* **104**: 1029–1035.

Barthe C, Asencio N, Lafore J, Chong M, Campistron B, Cazenave F. 2010. Multi-scale analysis of the 25–27 July 2006 convective period over Niamey: comparison between Doppler radar observations and simulations. *Q. J. R. Meteorol. Soc.* **136**(S1): 190–208.

Berry G. 2009. 'African easterly waves and convection'. PhD dissertation, Department of Atmospheric and Environmental Sciences, University at Albany, New York.

Berry G, Thorncroft C, Hewson T. 2007. African easterly waves during 2004: analysis using objective techniques. *Mon. Weather Rev.* **135**: 1251–1267.

Bluestein HB, Jain MH. 1985. Formation of mesoscale lines of precipitation: severe squall lines in Oklahoma during the Spring. *J. Atmos. Sci.* **42**: 1711–1732.

Bolton D. 1984. Generation and propagation of African squall lines. *Q. J. R. Meteorol. Soc.* **110**: 695–721.

Bosilovich MG, Schubert SD, Rienecker M, Todling R, Suarez M, Bacmeister J, Gelaro R, Kim G, Stajner I, Chen J. 2006. NASA's Modern Era Retrospective-Analysis for Research and Applications (MERRA). *US CLIVAR Variations* **4**(2): 5–8.

Browning KA, Wexler R. 1968. The determination of kinematic properties of a wind field using Doppler radar. *J. Appl. Meteorol.* **7**: 105–113.

Buarque SR, Sauvageot H. 1997. The estimation of rainfall in the Sahelian squall line by the area-threshold method. *Atmos. Res.* **43**: 207–216.

Burpee RW. 1972. The origin and structure of easterly waves in the lower troposphere of North Africa. *J. Atmos. Sci.* **29**: 77–90.

Burpee RW. 1974. Characteristics of North African easterly waves during the summers of 1968 and 1969. *J. Atmos. Sci.* **31**: 1556–1570.

Carlson TN. 1969a. Some remarks on African disturbances and their progress over the tropical Atlantic. *Mon. Weather Rev.* **97**(10): 716–726.

Carlson TN. 1969b. Synoptic histories of three African disturbances that developed into Atlantic hurricanes. *Mon. Weather Rev.* **97**: 256–276.

Chong M. 2009. The 11 August 2006 squall-line system as observed from MIT Doppler radar during the AMMA SOP. *Q. J. R. Meteorol. Soc.* **136**(S1): 209–226.

Chong M, Amayenc P, Scialom G, Testud J. 1987. A tropical squall line observed during the COPT 81 experiment in West Africa. Part 1. Kinematic structure inferred from dual-Doppler radar data. *Mon. Weather Rev.* **115**: 670–694.

Cifelli R, Nesbitt SW, Rutledge SA, Petersen WA, Yuter S. 2007. Radar characteristics of precipitation features in the EPIC and TEPPS regions of the East Pacific. *Mon. Weather Rev.* **135**: 1576–1595.

Cifelli R, Lang T, Rutledge SA, Guy N, Zipser EJ, Zawislak J, Holzworth R. 2010. Characteristics of an African easterly wave observed during NAMMA. *J. Atmos. Sci.* **67**: 3–25.

Coniglio MC, Stensrud DJ, Wicker LJ. 2006. Effects of upper-level shear on the structure and maintenance of strong quasi-linear mesoscale convective systems. *J. Atmos. Sci.* **63**: 1231–1252.

D'Amato N, Lebel T. 1998. On the characteristics of the rainfall events in the Sahel with a view to the analysis of climatic variability. *Int. J. Climatol.* **18**: 955–974.

DeLonge MS, Fuentes JD, Chan S, Kucera PA, Joseph E, Gaye AT, Daouda B. 2010. Attributes of mesoscale convective systems at the land–ocean transition in Senegal during NASA African Monsoon Multidisciplinary Analyses 2006. *J. Geophys. Res.* **115**: D10213, DOI: 201010.1029/2009JD012518.

DeMott CA, Rutledge SA. 1998. The vertical structure of TOGA COARE convection. Part I. Radar echo distributions. *J. Atmos. Sci.* **55**: 2730–2747.

Diedhiou A, Janicot S, Viltard A, de Felice P, Laurent H. 1999. Easterly wave regimes and associated convection over West Africa and tropical

Atlantic: results from the NCEP/NCAR and ECMWF reanalyses. *Climate Dyn.* **15**: 795–822.
Duvel JP. 1990. Convection over tropical Africa and the Atlantic Ocean during northern summer. Part II. Modulation by Easterly Waves. *Mon. Weather Rev.* **118**: 1855–1868.
Eldridge RH. 1957. A synoptic study of West African disturbance lines. *Q. J. R. Meteorol. Soc.* **84**: 468–469.
Fink AH, Reiner A. 2003. Spatiotemporal variability of the relation between African easterly waves and West African squall lines in 1998 and 1999. *J. Geophys. Res.* **108**: 4332, DOI: 200310.1029/2002JD002816.
Fink AH, Vincent DG, Ermert V. 2006. Rainfall types in the West African Sudanian Zone during the Summer Monsoon 2002. *Mon. Weather Rev.* **134**: 2143–2164.
Fortune M. 1980. Properties of African squall lines inferred from time-lapse satellite imagery. *Mon. Weather Rev.* **108**: 153–168.
Fuentes JD, Geerts B, Dejene T, D'Odorico P, Joseph E. 2008. Vertical attributes of precipitation systems in West Africa and adjacent Atlantic Ocean. *Theor. Appl. Climatol.* **92**: 181–193.
Gamache JF, Houze RAJ. 1982. Mesoscale air motions associated with a tropical squall line. *Mon. Weather Rev.* **110**: 118–135.
Geerts B, Dejene T. 2005. Regional and diurnal variability of the vertical structure of precipitation systems in Africa based on spaceborne radar data. *J. Climate* **18**: 893–916.
Gu G, Adler RF, Huffman GJ, Curtis S. 2004. African easterly waves and their association with precipitation. *J. Geophys. Res.* **109**: D04101, DOI: 200410.1029/2003JD003967.
Hamilton RA, Archbold JW, Douglas CKM. 1945. Meteorology of Nigeria and adjacent territory. *Q. J. R. Meteorol. Soc.* **71**: 231–264.
Hastenrath S. 1991. *Climate Dynamics of the Tropics*. Kluwer: Norwell, MA.
Hodges KI, Thorncroft CD. 1997. Distribution and statistics of African mesoscale convective weather systems based on the ISCCP Meteosat imagery. *Mon. Weather Rev.* **125**: 2821–2837.
Hopper LJ, Schumacher C. 2009. Baroclinicity influences on storm divergence and stratiform rain: subtropical upper-level disturbances. *Mon. Weather Rev.* **137**: 1338–1357.
Houze RA, Cheng C. 1977. Radar characteristics of tropical convection observed during GATE: mean properties and trends over the summer season. *Mon. Weather Rev.* **105**: 964–980.
Houze RA, Biggerstaff MI, Rutledge SA, Smull BF. 1989. Interpretation of Doppler weather radar displays of midlatitude mesoscale convective systems. *Bull. Am. Meteorol. Soc.* **70**: 608–619.
Hsieh J, Cook KH. 2005. A study of the energetics of African easterly waves using a regional climate model. *Mon. Weather Rev.* **133**: 1311–1327.
Hudlow MD. 1979. Mean rainfall patterns for the three phases of GATE. *J. Appl. Meteorol.* **18**: 1656–1669.
Kiladis GN, Thorncroft CD, Hall NMJ. 2006. Three-dimensional structure and dynamics of African easterly waves. Part I. Observations. *J. Atmos. Sci.* **63**: 2212–2230.
Laing AG, Fritsch JM. 1993. Mesoscale convective complexes in Africa. *Mon. Weather Rev.* **121**: 2254–2263.
Laing AG, Carbone R, Levizzani V, Tuttle J. 2008. The propagation and diurnal cycles of deep convection in northern tropical Africa. *Q. J. R. Meteorol. Soc.* **134**: 93–109.
Lang TJ, Nesbitt SW, Carey LD. 2009. On the correction of partial beam blockage in polarimetric radar data. *J. Atmos. Oceanic Technol.* **26**: 943–957.
Laurent H, D'Amato N, Lebel T. 1998. How important is the contribution of the mesoscale convective complexes to the Sahelian rainfall? *Phys. Chem. Earth* **23**: 629–633.
Le Barbé L, Lebel T. 1997. Rainfall climatology of the HAPEX-Sahel region during the years 1950–1990. *J. Hydrol.* **188**: 43–73.
Lebel T, Parker DJ, Flamant C, Bourlès B, Marticorena B, Mougin E, Peugeot C, Diedhiou A, Haywood JM, Ngamini JB, Polcher J, Redelsperger J, Thorncroft CD. 2010. The AMMA field campaigns: multiscale and multidisciplinary observations in the West African region. *Q. J. R. Meteorol. Soc.* **136**(S1): 8–33.
Liu C, Zipser EJ, Cecil DJ, Nesbitt SW, Sherwood S. 2008. A cloud and precipitation feature database from nine years of TRMM observations. *J. Appl. Meteorol. Climatol.* **47**: 2712–2728.
Lucas C, Zipser EJ, Ferrier BS. 2000. Sensitivity of tropical West Pacific oceanic squall lines to tropospheric wind moisture profiles. *J. Atmos. Sci.* **57**: 2351–2373.
McGarry MM, Reed RJ. 1978. Diurnal variations in convective activity and precipitation during phases II and III of GATE. *Mon. Weather Rev.* **106**: 101–113.
Machado LAT, Duvel J, Desbois M. 1993. Diurnal variations and modulation by easterly waves of the size distribution of convective cloud clusters over West Africa and the Atlantic Ocean. *Mon. Weather Rev.* **121**: 37–49.
Mapes BE, Houze RA. 1993a. Cloud clusters and superclusters over the oceanic warm pool. *Mon. Weather Rev.* **121**: 1398–1416.
Mapes B, Houze RA. 1993b. An integrated view of the 1987 Australian monsoon and its mesoscale convective systems. II. Vertical structure. *Q. J. R.Metereol. Soc.* **119**: 733–754.
Mapes BE, Houze RA. 1995. Diabatic divergence profiles in Western Pacific mesoscale convective systems. *J. Atmos. Sci.* **52**: 1807–1828.
Mapes BE, Lin J. 2005. Doppler radar observations of mesoscale wind divergence in regions of tropical convection. *Mon. Weather Rev.* **133**: 1808–1824.
Mathon V, Laurent H. 2001. Life cycle of Sahelian mesoscale convective cloud systems. *Q. J. R. Meteoreol. Soc.* **127**: 377–406.
Mathon V, Laurent H, Lebel T. 2002. Mesoscale convective system rainfall in the Sahel. *J. Appl. Meteorol. Climatol.* **41**: 1081–1092.
Mekonnen A, Thorncroft CD, Aiyyer AR. 2006. Analysis of convection and its association with African easterly waves. *J. Climate* **19**: 5405–5421.
Mohr CG, Jay Miller L, Vaughan RL, Frank HW. 1986. The merger of mesoscale datasets into a common cartesian format for efficient and systematic analyses. *J. Atmos. Ocean. Technol.* **3**: 143–161.
Mohr KI. 2004. Interannual, monthly, and regional variability in the wet season diurnal cycle of precipitation in sub-Saharan Africa. *J. Climate* **17**: 2441–2453.
Mohr KI, Thorncroft CD. 2006. Intense convective systems in West Africa and their relationship to the African easterly jet. *Q. J. R. Meteorol. Soc.* **132**: 163–176.
Mohr KI, Famiglietti JS, Zipser EJ. 1999. The contribution to tropical rainfall with respect to convective system type, size, and intensity estimated from the 85-GHz ice-scattering signature. *J. Appl. Meteor.* **38**: 596–606.
Mohr KI, Molinari J, Thorncroft CD. 2009. The interannual stability of cumulative frequency distributions for convective system size and intensity. *J. Climate* **22**: 5218–5231.
Nesbitt SW, Zipser EJ, Cecil DJ. 2000. A census of precipitation features in the Tropics using TRMM: radar, ice scattering, and lightning observations. *J. Climate* **13**: 4087–4106.
Nesbitt SW, Cifelli R, Rutledge SA. 2006. Storm morphology and rainfall characteristics of TRMM precipitation features. *Mon. Weather Rev.* **134**: 2702–2721.
Nicholls SD, Mohr KI. 2010. An analysis of the environments of intense convective systems in West Africa in 2003. *Mon. Weather Rev.* **138**: 3721–3739.
Nieto Ferreira R, Rickenbach T, Guy N, Williams E. 2009. Radar observations of convective system variability in relationship to African easterly waves during the 2006 AMMA Special Observing Period. *Mon. Weather Rev.* **137**: 4136–4150.
Nuret M, Lafore J, Guichard F, Redelsperger J, Bock O, Agusti-Panareda A, N'Gamini J. 2008. Correction of humidity bias for Vaisala RS80-A sondes during the AMMA 2006 observing period. *J. Atmos. Ocean. Technol.* **25**: 2152–2158.
Nzeukou A, Sauvageot H, Ochou AD, Kebe CMF. 2004. Raindrop size distribution and radar parameters at Cape Verde. *J. Appl. Meteor. Climatol.* **43**: 90–105.
Patterson VL, Hudlow MD, Pytlowaney PJ, Richards FP, Hoff JD. 1979. 'GATE radar rainfall processing system'. NOAA Technical Memo, Springfield, VA.
Payne SW, McGarry MM. 1977. The relationship of satellite inferred convective activity to easterly waves over West Africa and the adjacent ocean during phase III of GATE. *Mon. Weather Rev.* **105**: 413–420.
Peters M, Tetzlaff G. 1988. The structure of West African squall lines and their environmental moisture budget. *Meteor. Atmos. Phys.* **39**: 74–84.
Redelsperger J, Diongue A, Diedhiou A, Ceron J, Diop M, Gueremy J, Lafore J. 2002. Multi-scale description of a Sahelian synoptic weather system representative of the West African monsoon. *Q. J. R. Meteor. Soc.* **128**: 1229–1257.
Redelsperger J, Thorncroft CD, Diedhiou A, Lebel T, Parker DJ, Polcher J. 2006. African Monsoon Multidisciplinary Analysis: an international research project and field campaign. *Bull. Am. Meteorol. Soc.* **87**: 1739–1746.
Reed RJ, Norquist DC, Recker EE. 1977. The structure and properties of African wave disturbances as observed during Phase III of GATE. *Mon. Weather Rev.* **105**: 317–333.
Rickenbach T, Nieto Ferreira R, Guy N, Williams E. 2009. Radar-observed squall line propagation and the diurnal cycle of convection in Niamey, Niger, during the 2006 African Monsoon and Multidisciplinary Analyses Intensive Observing Period. *J. Geophys. Res.* **114**: D03107, DOI: 200910.1029/2008JD010871.
Rienecker MM, Suarez MJ, Todling R, Bacmeister J, Takacs L, Liu H, Gu W, Sienkiewicz M, Koster RD, Gelaro R, Stajner I, Nielsen JE. 2008.

The GEOS-5 Data Assimilation System: Documentation of Versions 5.0.1 and 5.1.0. NASA GSFC Technical Report Series on Global Modeling and Data Assimilation. NASA: Hanover, MD. Available: http://gmao.gsfc.nasa.gov/pubs/docs/GEOS5_104606-Vol27.pdf.

Roux F. 1988. The West African squall line observed on 23 June 1981 during COPT 81: kinematics and thermodynamics of the convective region. *J. Atmos. Sci.* **45**: 406–426.

Roux F, Ju S. 1990. Single-Doppler observations of a West African squall line on 27–28 May 1981 during COPT 81: kinematics, thermodynamics and water budget. *Mon. Weather Rev.* **118**: 1826–1854.

Sall SM, Sauvageot H. 2005. Cyclogenesis off the African coast: the case of Cindy in August 1999. *Mon. Weather Rev.* **133**: 2803–2813.

Sauvageot H, Lacaux J. 1995. The shape of averaged drop size distributions. *J. Atmos. Sci.* **52**: 1070–1083.

Schumacher C, Houze RA. 2003. Stratiform rain in the Tropics as seen by the TRMM precipitation radar. *J. Climate* **16**: 1739–1756.

Schumacher C, Houze RA. 2006. Stratiform precipitation production over sub-Saharan Africa and the tropical East Atlantic as observed by TRMM. *Q. J. R. Meteorol. Soc.* **132**: 2235–2255.

Shinoda M, Okatani T, Saloum M. 1999. Diurnal variations of rainfall over Niger in the West African Sahel: a comparison between wet and drought years. *Int. J. Climatol.* **19**: 81–94.

Steiner M, Houze RA, Yuter SE. 1995. Climatological characterization of three-dimensional storm structure from operational radar and rain gauge data. *J. Appl. Meteorol.* **34**: 1978–2007.

Taleb EH, Druyan LM. 2003. Relationships between rainfall and West African wave disturbances in station observations. *Int. J. Climatol.* **23**: 305–313.

Thorncroft CD, Hall NMJ, Kiladis GN. 2008. Three-dimensional structure and dynamics of African easterly waves. Part III. Genesis. *J. Atmos. Sci.* **65**: 3596–3607.

Weisman ML, Klemp JB. 1982. The dependence of numerically simulated convective storms on vertical wind shear and buoyancy. *Mon. Weather Rev.* **110**: 504–520.

Weisman ML, Klemp JB, Rotunno R. 1988. Structure and evolution of numerically simulated squall lines. *J. Atmos. Sci.* **45**: 1990–2013.

Zipser EJ, Twohy CH, Tsay S, Hsu NC, Heymsfield GM, Thornhill KL, Tanelli S, Ross R, Krishnamurti TN, Ji Q, Jenkins G, Ismail S, Ferrare R, Chen G, Browell EV, Anderson B, Hood R, Goodman HM, Heymsfield A, Halverson J, Dunion JP, Douglas M, Cifelli R. 2009. The Saharan air layer and the fate of African easterly waves: NASA's AMMA field study of tropical cyclogenesis. *Bull. Am. Meteorol. Soc.* **90**: 1137–1156.

